



LETTER

In vivo coherent anti-Stokes Raman scattering microscopy reveals vitamin A distribution in the liver

Marko Rodewald^{1,2}  | Hyeonsoo Bae²  | Sophie Huschke^{3,4} |
 Tobias Meyer-Zedler^{1,2}  | Michael Schmitt¹  | Adrian Tibor Press^{3,4,5}  |
 Stephanie Schubert⁶  | Michael Bauer^{3,4}  | Juergen Popp^{1,2*} 

¹Institute of Physical Chemistry and Abbe Center of Photonics, Friedrich Schiller University, Jena, Germany

²Leibniz Institute of Photonic Technology, Member of Leibniz Health Technologies, Jena, Germany

³Department of Anesthesiology and Intensive Care Medicine, Jena University Hospital, Jena, Germany

⁴Center for Sepsis Control and Care, Jena University Hospital, Jena, Germany

⁵Faculty of Medicine, Friedrich Schiller University, Jena, Germany

⁶Institute of Pharmacy, Department of Pharmaceutical Technology and Biopharmacy, Friedrich Schiller University, Jena, Germany

***Correspondence**

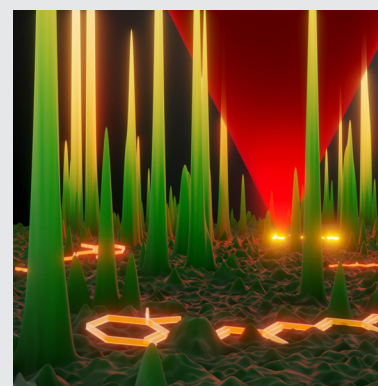
Juergen Popp, Leibniz Institute of Photonic Technology, Albert-Einstein-Straße 9, 07743, Jena, Germany.
 Email: juergen.popp@ipht-jena.de

Funding information

German Research Foundation (DFG), Grant/Award Number: 316213987

Abstract

Here we present a microscope setup for coherent anti-Stokes Raman scattering (CARS) imaging, devised to specifically address the challenges of *in vivo* experiments. We exemplify its capabilities by demonstrating how CARS microscopy can be used to identify vitamin A (VA) accumulations in the liver of a living mouse, marking the positions of hepatic stellate cells (HSCs). HSCs are the main source of extracellular matrix protein after hepatic injury and are therefore the main target of novel nanomedical strategies in the development of a treatment for liver fibrosis. Their role in the VA metabolism makes them an ideal target for a CARS-based approach as they store most of the body's VA, a class of compounds sharing a retinyl group as a structural motive, a moiety that is well known for its exceptionally high Raman cross section of the C=C stretching vibration of the conjugated backbone.

**KEYWORDS**

coherent anti-stokes Raman scattering, hepatic stellate cells, liver fibrosis, multimodal nonlinear microscopy, vitamin A

1 | INTRODUCTION

The liver carries out major metabolic and immunologic functions. Among its metabolic functions is the vitamin A (VA) uptake, storage and release, protecting the organism from the consequences of toxic VA doses. Physiologically, VA is a nutrient essential for health as it regulates,

for example, epithelial growth and immunological processes. Hepatic stellate cells (HSCs) in the liver constitute the main storage site for VA [1, 2]. Following hepatic injury, however, HSCs are activated and lose their intracellular VA storages, which leads to their transformation into collagen-producing myofibroblasts [3]. Governing the excretion of excess extracellular matrix protein, such

This is an open access article under the terms of the Creative Commons Attribution-NonCommercial License, which permits use, distribution and reproduction in any medium, provided the original work is properly cited and is not used for commercial purposes.

© 2021 The Authors. *Journal of Biophotonics* published by Wiley-VCH GmbH.

activated HSCs are the most relevant cell type in the development of liver fibrosis to which there is currently no treatment available. According to the World Health Organization, in 2016, liver cirrhosis, the final stage of liver fibrosis, was the fourth leading cause of death worldwide in the age group 50 to 59 [4], creating a strong incentive for the development of novel treatment strategies and theranostic approaches. One such strategy that has sparked interest recently is the application of nanoparticles (NPs) [5, 6] and other nanoscale functional materials as cell-selective carriers for the targeted delivery of drugs. The primary target of such systems are HSCs, given their specific role in fibrosis. Studying the uptake and accumulation dynamics, as well as the final fate of NPs inside the liver of a living animal and proving a selectiveness for HSCs will require a method of identifying HSCs *in vivo*. However, the detection of HSCs is challenging, due to the incompatibility of histopathological staining techniques with *in vivo* measurements. Thus, an appropriate method should be fast, providing constant feedback during, for example, time-resolved nanocarrier/drug-focused measurements and minimizing artifacts due to the unavoidable sample movement caused, for example, by breathing or the heartbeat. Furthermore, it should, ideally, allow for simultaneous recording of separate images to combine the HSC identification with further modalities, such as fluorescence, for instance for marker detection. So far, no procedure was reported fulfilling all these requirements. UV excited fluorescence microscopy [7–9] and linear Raman spectroscopy [10, 11] have been employed to address HSCs in liver tissue but fail to meet these aforementioned criteria. VA excitation with UV light leads to rapid photobleaching [7–9, 12] within seconds of illumination, preventing any prolonged measurements of the same sample area, making this method ineffective for kinetic measurements. Linear Raman based methods suffer from the inefficiency of the weak Raman process leading to long acquisition times incompatible with *in vivo* measurements of larger sample areas [13].

Here, we demonstrate, for the first time, the identification of HSCs by coherent anti-Stokes Raman scattering (CARS) microscopy in a living mouse, utilizing the stellate cell's role in the VA metabolism by measuring spectrally resolved CARS images in the C=C stretching vibration. The high Raman cross section of this vibration renders VA the perfect target for Raman-based methods, such as CARS. The viability of this approach had been demonstrated before in our group on excised tissue [14] but wasn't extended to *in vivo* measurements and the specific challenges associated with them, the most notable among which are the limited time window, sample movement and the need for an epi detection scheme.* To meet these challenges we designed an inverted microscope setup providing a modular all-epi detection scheme with up to three easily customizable detection

channels. An appropriate data analysis procedure was developed and is exemplified in this study.

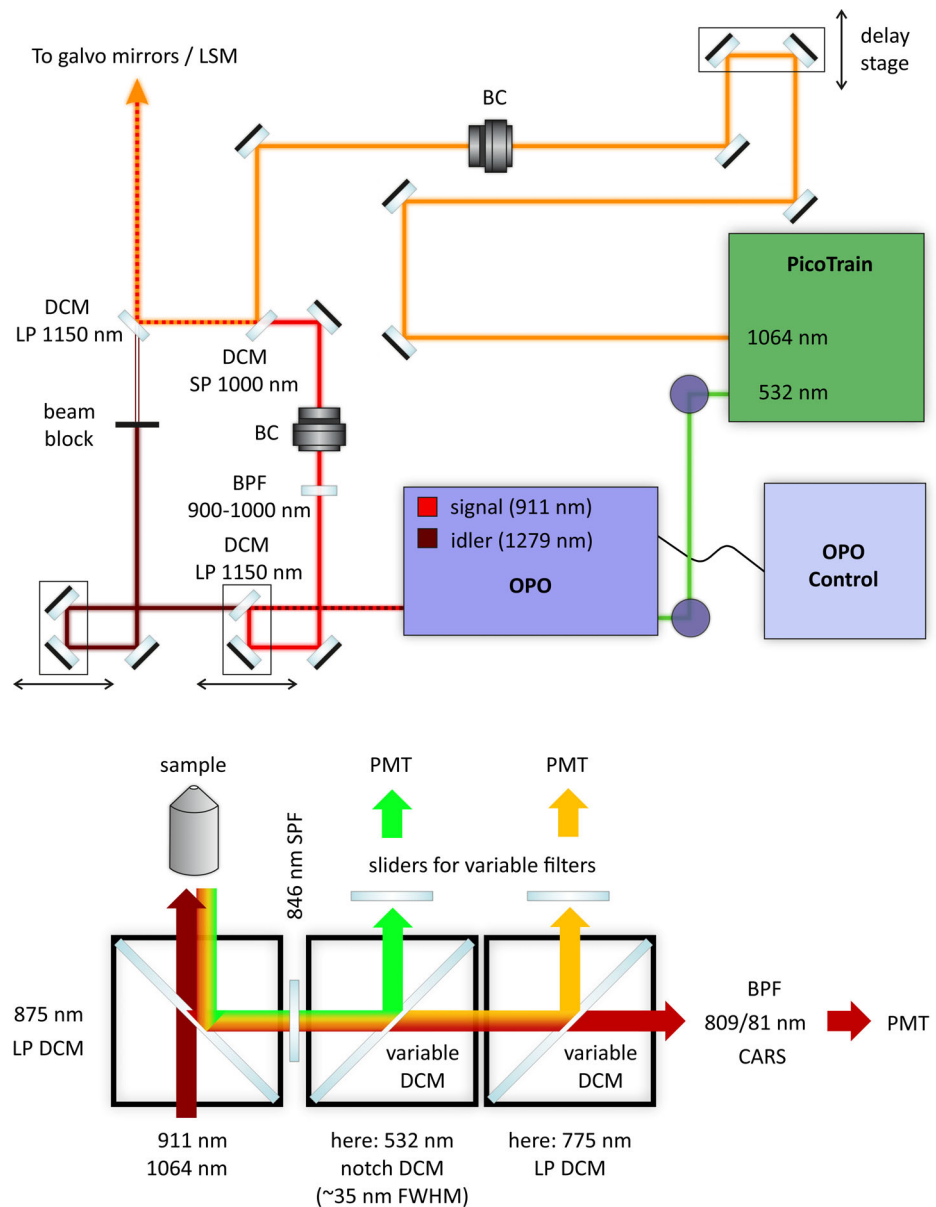
Besides a reliable localization of HSCs via CARS, the approach presented in this contribution would also provide the option to use the other non-linear effects inherently induced by the CARS lasers, namely two-photon excited fluorescence (TPEF) and second harmonic generation, in a multimodal imaging approach to monitor collagen on the liver surface, the organs autofluorescence [14] or, as discussed above, to perspectively track labeled drugs or drug carrier materials aimed at HSCs.

2 | EXPERIMENTAL

2.1 | Imaging setup and parameters

For *in vivo* measurements of CARS from HSCs a home-built microscope, the general layout of which was previously described in detail [15], was used but modified to meet the needs of *in vivo* imaging, most importantly by converting it into an inverted microscope with an epi-detection scheme. Differing from its original description [15], the setup uses a mode locked Nd:vanadate laser source (High-Q picoTrain, High-Q Laser, Austria), generating short pulses of 7.5 ps, centered at 1064 nm, at a repetition rate of 80 MHz which comprise the Stokes beam in this setup. As a second output, the laser provides frequency-doubled pulses which are used to pump an optical parametric oscillator (OPO, Levante Emerald, A.P.E. Germany) to generate the desired pump wavelength for the CARS process. For the purpose of this work, the OPO was set to generate wavelengths between 909.1 and 913.9 nm with an increment of 0.2 nm, corresponding to Raman resonances between 1601 and 1544 cm^{-1} . The fundamental output of the Nd:vanadate laser is passed through a delay stage to achieve temporal overlap of the pump and Stokes beam and is then combined with the pump beam by a dichroic mirror. The temporally and spatially overlapped pump and Stokes beams are passed onto a set of scanning galvo mirrors which direct the beams through a tube and scanning lens onto the back aperture of an objective lens (0.4 NA, M Plan Apo NIR 20X, Mitutoyo, Japan). Average powers at the sample were around 155 mW (pump) and 135 mW (Stokes). The generated CARS signal (793.6–800.9 nm) is collected in epi direction by the same objective and separated from the excitation lasers and cleaned by appropriate dichroic mirrors and optical filters before being detected using a photomultiplier tube (H10721-20, Hamamatsu, Japan). A schematic of the beam pass and detection scheme, including all dichroic mirrors and filters, is provided in Figure 1. Due to time constraints inherent to the *in vivo* experiment, the average pump beam power

FIGURE 1 Overview of the beam path (top) and detection scheme (bottom) of the microscope. BC, Berek compensator; BPF, band pass filter, DCM, dichroic mirror; LP, long pass; LSM, laser scanning microscope; OPO, optic parametric oscillator; PMT, photo multiplier tube; SPF, short pass filter. All dichroic mirrors and filters can be changed quickly and easily to adjust for specific experiments or different wavelengths than the ones used in this study



which slightly varies between different pump wavelengths due to more or less efficient generation could not be adjusted to ensure perfectly consistent average powers between measurements. This problem was addressed in the data processing stage by a suitable normalization. Images were recorded at $1024 \text{ px} \times 1024 \text{ px}$ at 16 bits/px in a field of view of $400 \mu\text{m} \times 400 \mu\text{m}$ and with a pixel dwell time of $2 \mu\text{s}$. Five frames were averaged for each image.

2.2 | Animal treatment and sample preparation

A male FVB/N mouse was used in this study. The animal was maintained at the animal facility of the Jena University Hospital under artificial day-night cycles (12 hour

light-dark cycles; 23°C room temperature; 30% to 60% environment humidity) in a pathogen-free environment. The study was conducted in accordance with the German legislation on the protection of animals and with permission of the Thuringian state administrative office.

During all procedures and imaging methods, the animal remained under deep general anesthesia using 1% to 2% isoflurane (CP-Pharma, Germany) and 5 mg kg^{-1} body weight *per os* meloxicam (0.5 mg mL^{-1} suspension, CP-Pharma, Germany) for additional pain relief. Pain-reflexes were assessed to gauge the depth of anesthesia. Still under anesthesia, the animal was sacrificed at the end of the experiments. For *in vivo* microscopy, a tail-vein catheter (30 G) was placed. The liver was exposed by an abdominal incision and the animal was carefully placed on a microscope stage equipped with a $170 \mu\text{m}$ glass

bottom plate. The exposed organ was kept moist throughout the measurements to limit drying artifacts. A heat lamp was applied to avoid hypothermia.

3 | RESULTS AND DISCUSSION

As discussed in the introduction, HSCs do not only store most of the body's VA but are also the most relevant cell type in the development of liver fibrosis as they govern the excretion of excess collagen. A reliable identification of HSCs in native liver tissue is thus of utmost importance. We, therefore, explored the potential of CARS microscopy for the identification of HSCs. Figure 2 shows three of 25 spectrally resolved CARS images obtained from surface-near layers of the liver of a living mouse at pump wavelengths corresponding to wavenumbers of 1584.5 cm^{-1} (highest CARS intensity) and 1601.4 or 1543.6 cm^{-1} (highest and lowest addressed wavenumber). The central image clearly shows a number of bright dots that are absent or significantly weaker in the other two images. Linear Raman measurements of endogenous VA in native mouse liver tissue were reported to have shown a strong Raman response of the conjugated C=C double bonds of the retinyl unit at approximately 1594 cm^{-1} (1595 cm^{-1} [16] and 1593 cm^{-1} [11]). This suggests that the bright dots can be attributed to VA accumulations, thus indicating the position of HSCs. To prove this assumption a thorough spectral analysis was performed on the whole data set, as - due to the nature of CARS - the Raman resonance frequency is not directly comparable to the (beating) frequency at which the highest CARS signal occurs.

One of the major challenges associated with *in vivo* imaging, if quantitative spatio-temporal relations are to be monitored (or maintained), is motion artifacts. Those artifacts can arise, for example, due to breathing, the heartbeat and global sample drift and are facilitated by the soft nature of healthy liver tissue. The occurring artifacts are oftentimes not well accounted for by simple translational and rotational transformations, making correcting for them in data sets that were recorded over the span of several minutes rather challenging. Though motion artifacts were small in the here presented data set, they still required correction to assure that the same areas are compared at different wavenumbers. Therefore, the raw images were subjected to a stack alignment procedure using ImageJ (v.1.52v) [17] and the bUnwarpJ plugin [18] which performs image registration by elastic deformations based on B-splines. The plugin, by default, handles only pairs of images. For that reason a macro was written that extends the capabilities of the bUnwarpJ plugin to stacks of images by generating pairs of every slice and either a moving reference or a fixed reference. For the purposes of this work, a fixed reference was chosen (slice 9, $\lambda_{\text{pump}} = 910.7\text{ nm}$). The macro code (Document S1) and details are provided as part of the supporting information Data S1. Figure 3A shows a maximum intensity projection of all 25 spectrally resolved measurements of the liver of a living mouse after stack unwarping. None of the bright dots appear severely elongated or smeared out, indicating a successful unwarping.

For the identification and analysis of bright dots, a purpose-made ImageJ macro (code [Document S2] and details provided in the supporting information Data S1) was developed which separates “dots” and “non-dot”-

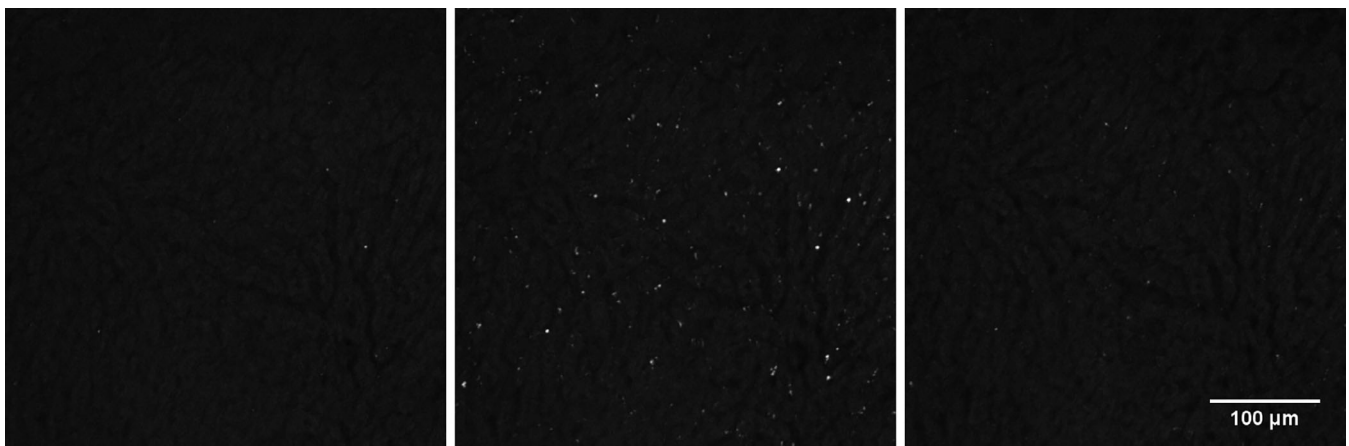


FIGURE 2 In vivo coherent anti-Stokes Raman scattering (CARS) images of a mouse liver, recorded at pump wavelengths corresponding to 1601.4 cm^{-1} (left), 1584.5 cm^{-1} (middle) and 1543.6 cm^{-1} (right). Bright dots indicate VA accumulations and mark the positions of HSCs. The data are represented in linear gray scale, starting from the global minimum (black) to the global maximum (white). The typical sponge-like microarchitecture of the liver is visible in the non-resonant background signal. A mosaic of all 25 unprocessed, spectrally resolved CARS images from which the above ones were selected is part of the supporting information Data S1 (Figure S1)

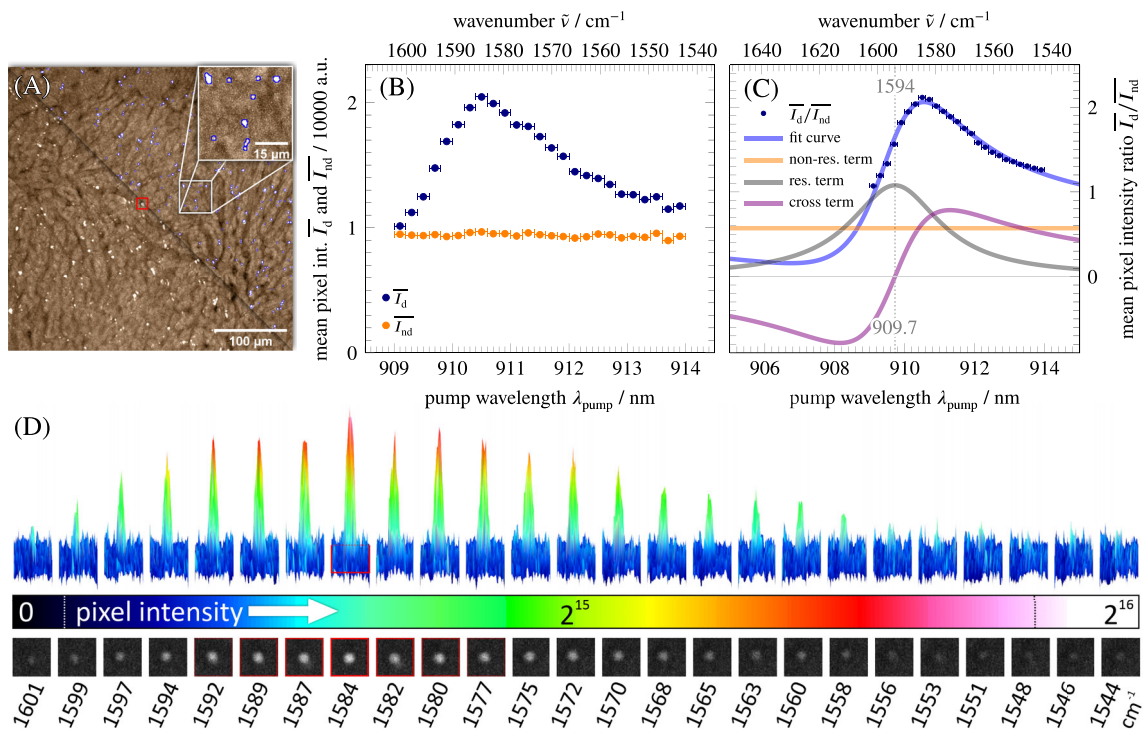


FIGURE 3 *In vivo* CARS measurements of retinoids in surface near layers of murine liver tissue. A, Maximum intensity projection (MIP) of a stack of CARS images recorded at different pump wavelengths corresponding to resonance conditions between 1540 and 1600 cm^{-1} . To account for motion artifacts, the stack underwent a stack alignment procedure prior to MIP. Areas rich in retinoids show as bright dots and mark HSCs. Blue outlines (top right half) indicate areas identified as dots by a dot identification algorithm. Masks generated from the results of that algorithm were projected to the individual slices (see Data S1 for details). B, Mean pixel intensities in dot (I_d) and non-dot (I_{nd}) areas over the pump wavelength and respective wavenumbers. C, Ratio of mean pixel intensities of dot and non-dot areas over the pump wavelength and respective wavenumbers, alongside with a corresponding fit curve and its components. The raw data plotted in B and C, are available in the supporting information Data S1. D, Pixel intensities of a single dot in the raw images (before stack alignment, approximate position indicated in MIP image by red square) in 2.5 D color coded and 2 D gray scale representation. Minimum and maximum values are indicated by dotted lines

areas and calculates the mean pixel intensities \bar{I}_d and \bar{I}_{nd} in the respective areas. Figure 3B shows the mean pixel intensities in dot and non-dot regions. There is no appreciable spectral signature of VA in the areas classified as not belonging to HSCs, whereas the spectral signature is very prominent in the areas identified as belonging to HSCs, indicating an almost complete registration of all HSC areas, while an overly lax assignment of any area to the HSC category can be easily ruled out upon visual inspection of areas marked by blue outlines in Figure 3A. Since varying pump beam intensities due to different generation efficiencies of the OPO at different wavelengths could not be addressed experimentally because of the time constraints imposed by the *in vivo* experiments, it was made use of the fact that both, four-wave mixing signal from non-dot areas, as well as CARS signal from dot areas depend on the square of the pump beam intensity, by dividing the mean pixel intensities in dot areas by the mean pixel intensity in non-dot areas. Plotting the resulting ratios over the respective pump

wavelength yields the CARS spectrum (data points in Figure 3C).

The spectrally resolved CARS data (\bar{I}_d/\bar{I}_{nd}) were then fitted to extract information about the individual components adding up to the overall CARS intensity $I(\lambda_p)$ and, most importantly, the resonance wavenumber. A detailed derivation of the fitting function is part of the supporting information Data S1. Briefly, the relation

$$I(\lambda_p) \propto \chi_{NR}^{(3)2} + \frac{A_R^2}{d} + \frac{4\pi c \chi_{NR}^{(3)} A_R \left(\frac{1}{\lambda_{p,res}} - \frac{1}{\lambda_p} \right)}{d}, \quad (1)$$

with

$$d = 4\pi^2 c^2 \left(\frac{1}{\lambda_{p,res}} - \frac{1}{\lambda_p} \right)^2 + \Gamma^2, \quad (2)$$

was used, where $\chi_{NR}^{(3)}$ is the constant non-resonant contribution, A_R the normalized vibrational mode strength, Γ

the bandwidth of the Raman line and $\lambda_{p,res}$ the pump wavelength at which Raman resonance occurs. Relation (1) was converted into an equality by introducing a constant factor k to the right-hand side of the equation, leading to Equation (3),

$$I(\lambda_p) = \chi'_{NR}{}^{(3)2} + \frac{A'_R{}^2}{d} + \frac{4\pi c \chi'_{NR}{}^{(3)} A'_R \left(\frac{1}{\lambda_{p,res}} - \frac{1}{\lambda_p} \right)}{d}, \quad (3)$$

where $\chi'_{NR}{}^{(3)} = \sqrt{k} \cdot \chi_{NR}{}^{(3)}$ and $A'_R = \sqrt{k} \cdot A_R$. The nonlinear curve fit was performed in OriginPro 9.0 [19], using a $\Delta\chi^2_{red}$ of 10^{-15} between successive iterations as convergence criterion and with unknown fitting parameters $\chi'_{NR}{}^{(3)}$, A'_R , $\lambda_{p,res}$ and Γ .

From the fit (Figure 3C) the highest CARS intensity was determined to be at $\sim 1584 \text{ cm}^{-1}$ and the resonance was determined to be at $\sim 1594 \text{ cm}^{-1}$. This is in agreement with the above-cited values for VA from linear Raman measurements and confirms earlier results on excised tissue [14]. As it is known that Raman spectra of HSCs are dominated by VA, while surrounding liver tissue does not show any bands around 1594 cm^{-1} in spectra recorded with the same S/N ratio [11], finding this resonance is sufficient to confirm the identification of HSCs. Furthermore, no compounds other than VA which also have long conjugated double bond systems are expected to accumulate in agglomerates like the observed ones of 1 to 3 μm . The storage of VA in lipid droplets of this size, on the other hand, is very well known and strict colocalization has been documented [14]. The obtained results render this approach highly attractive for *in vivo* applications in which, for example, the positions of fluorescence labeled drug delivery systems, such as NPs, have to be tracked in time relative to HSCs. We suggest a two-step procedure in such a scenario: first, three measurements are taken, one at the wavenumber with the highest CARS intensity and one off-resonance measurement in each direction which should suffice for reliable HSC identification. In our particular case this amounts to a total time requirement of 3 minutes, about 2.1 s/frame \cdot 5 frames \cdot 3 = 31.5 s of which were actual measurement time, the rest accounts for manually changing the pump wavelength and saving the measured data. This is typically not detrimental and therefore in line with the specific requirements of *in vivo* experiments. Second, simultaneous CARS/TPEF measurements at the wavenumber of the highest CARS intensity are taken after administration of the labeled agent. The CARS images in this case would allow to account for sample movement and therefore address one of the major difficulties in imaging live specimens.

4 | CONCLUSIONS

In view of the important role of HSCs in the development and progression of liver fibrosis as the main source of extracellular matrix protein in the liver, we investigated the potential of CARS microscopy for identifying them in the complex organ matrix. We found that spectrally resolved CARS can be used to localize HSCs *in vivo* based on their VA signature. Spectral analysis allowed us to identify the wavenumber of highest CARS intensity (1584 cm^{-1}) and the resonance wavenumber (1594 cm^{-1}). Not relying on any of the other modalities induced by the CARS lasers would allow utilizing them to, simultaneously, for example, measure collagen on the liver surface and either autofluorescence from the organ or labeled drugs/functional nano-materials, targeted at HSCs.

ACKNOWLEDGMENTS

This study was funded by the German Research Foundation (DFG) through the Collaborative Research Centre PolyTarget 1278 “Polymer-based nanoparticle libraries for targeted anti-inflammatory strategies” (project C01) under DFG project number 316213987. Open Access funding enabled and organized by ProjektDEAL.

CONFLICT OF INTEREST

The authors have no potential conflicts of interest to declare.

DATA AVAILABILITY STATEMENT

Data available on request from the authors.


ORCID

Marko Rodewald  <https://orcid.org/0000-0001-9021-8270>

Hyeonsoo Bae  <https://orcid.org/0000-0002-2965-2729>

Tobias Meyer-Zedler  <https://orcid.org/0000-0001-6740-629X>

Michael Schmitt  <https://orcid.org/0000-0002-3807-3630>

Adrian Tibor Press  <https://orcid.org/0000-0002-6089-6764>

Stephanie Schubert  <https://orcid.org/0000-0001-9527-7763>

Michael Bauer  <https://orcid.org/0000-0002-1521-3514>

Juergen Popp  <https://orcid.org/0000-0003-4257-593X>

ENDNOTE

* *In vivo* experiments on macroscopic animals inherently deal with bulky (non-transparent) samples that prohibit forward detection schemes. Modalities like CARS, the generation of which is typically more efficient in forward direction, have to rely on stochastic backscattering to a large degree, in combination with an epi detection scheme as a less efficient alternative.

REFERENCES

- [1] R. Blomhoff, *Vitamin A in Health and Disease*, Vol. 1, Chapman and Hall/CRC, Boca Raton **1994**.
- [2] W. S. Blaner, H. F. Hendriks, A. Brouwer, A. M. de Leeuw, D. L. Knook, D. S. Goodman, *J. Lipid Res.* **1985**, *26*(10), 1241.
- [3] S. L. Friedman, *Physiol. Rev.* **2008**, *88*(1), 125.
- [4] World Health Organization. https://www.who.int/gho/mortality_burden_disease/causes_death/top_10/en/.
- [5] Z. Zhang, C. Wang, Y. Zha, W. Hu, Z. Gao, Y. Zang, J. Chen, J. Zhang, L. Dong, *ACS Nano* **2015**, *9*(3), 2405.
- [6] P. Klemm, S. Huschke, M. Rodewald, N. Ehteshamzad, M. Behnke, X. Wang, G. Cinar, I. Nischang, S. Hoepfener, C. Weber, A. T. Press, C. Höppener, T. Meyer, V. Deckert, M. Schmitt, J. Popp, M. Bauer, S. Schubert, *Polym. Chem.* **2021**, *12* (6), 911.
- [7] M. Bauer, N. C. Paquette, J. X. Zhang, I. Bauer, B. H. J. Pannen, S. R. Kleeberger, M. G. Clemens, *Hepatology* **1995**, *22* (5), 1565.
- [8] N. Higashi, H. Senoo, *Anat. Rec. A Discov. Mol. Cell. Evol. Biol.* **2003**, *271*(1), 240.
- [9] B. Vollmar, S. Siegmund, M. D. Menger, *Hepatology (Baltimore, MD)* **1998**, *27*(6), 1544.
- [10] K. Galler, F. Schleser, E. Fröhlich, R. P. Requardt, A. Kortgen, M. Bauer, J. Popp, U. Neugebauer, *Integr. Biol.* **2014**, *6*(10), 946.
- [11] K. Galler, R. P. Requardt, U. Glaser, R. Markwart, T. Bocklitz, M. Bauer, J. Popp, U. Neugebauer, *Sci. Rep.* **2016**, *6*, 24155.
- [12] H. Popper, *Physiol. Rev.* **1944**, *24*(2), 205.
- [13] K. Eberhardt, C. Stiebing, C. Matthäus, M. Schmitt, J. Popp, *Expert Rev. Mol. Diagn.* **2015**, *15*(6), 773.
- [14] F. B. Legesse, S. Heuke, K. Galler, P. Hoffmann, M. Schmitt, U. Neugebauer, M. Bauer, J. Popp, *Chemphyschem* **2016**, *17* (24), 4043.
- [15] T. Meyer, M. Baumgartl, T. Gottschall, T. Pascher, A. Wuttig, C. Matthäus, B. F. M. Romeike, B. R. Brehm, J. Limpert, A. Tünnermann, O. Guntinas-Lichius, B. Dietzek, M. Schmitt, J. Popp, *Analyst* **2013**, *138*(14), 4048.
- [16] K. Kochan, K. M. Marzec, E. Maslak, S. Chlopicki, M. Baranska, *Analyst* **2015**, *140*(7), 2074.
- [17] J. Schindelin, I. Arganda-Carreras, E. Frise, V. Kaynig, M. Longair, T. Pietzsch, S. Preibisch, C. Rueden, S. Saalfeld, B. Schmid, J.-Y. Tinevez, D. J. White, V. Hartenstein, K. Eliceiri, P. Tomancak, A. Cardona, *Nat. Methods* **2012**, *9*(7), 676.
- [18] I. Arganda-Carreras, C. O. S. Sorzano, R. Marabini, J. M. Carazo, C. Ortiz-de Solorzano, J. Kybic, in *Computer Vision Approaches to Medical Image Analysis*, Vol. 4241 (Eds: D. Hutchison, T. Kanade, J. Kittler, J. M. Kleinberg, F. Mattern, J. C. Mitchell, M. Naor, O. Nierstrasz, C. P. Rangan, B. Steffen, M. Sudan, D. Terzopoulos, D. Tygar, M. Y. Vardi, G. Weikum, R. R. Beichel, M. Sonka), Springer Berlin Heidelberg, Berlin, Heidelberg **2006**, p. 85.
- [19] Origin(Pro), Version 2020. OriginLab Corporation, Northampton, MA, USA. % This file was created with Citavi 6.4.0.35.

SUPPORTING INFORMATION

Additional supporting information may be found online in the Supporting Information section at the end of this article.

How to cite this article: Rodewald M, Bae H, Huschke S, et al. *In vivo* coherent anti-Stokes Raman scattering microscopy reveals vitamin A distribution in the liver. *J. Biophotonics*. 2021;14: e202100040. <https://doi.org/10.1002/jbio.202100040>